

## HERSCHEL OBSERVATIONS OF THE W3 GMC: CLUES TO THE FORMATION OF CLUSTERS OF HIGH-MASS STARS

A. RIVERA-INGRAHAM,<sup>1,2,3</sup> P. G. MARTIN,<sup>4</sup> D. POLYCHRONI,<sup>5</sup> F. MOTTE,<sup>6</sup> N. SCHNEIDER,<sup>6,7,8</sup> S. BONTEMPS,<sup>7,8</sup> M. HENNEMANN,<sup>6</sup> A. MENSCHIKOV,<sup>6</sup> Q. NGUYEN LUONG,<sup>4</sup> PH. ANDRÉ,<sup>6</sup> D. ARZOUMANIAN,<sup>6</sup> J.-PH. BERNARD,<sup>3</sup> J. DI FRANCESCO,<sup>9,10</sup> D. ELIA,<sup>11</sup> C. FALLSCHEER,<sup>10,9</sup> T. HILL,<sup>6</sup> J. Z. LI,<sup>12</sup> V. MINIER,<sup>6</sup> S. PEZZUTO,<sup>11</sup> A. ROY,<sup>4</sup> K. L. J. RYGL,<sup>11</sup> S. I. SADAVOY,<sup>10,9</sup> L. SPINOGLIO,<sup>11</sup> G. J. WHITE,<sup>13,14</sup> C. D. WILSON<sup>15</sup>

Draft version February 24, 2022

## ABSTRACT

The W3 GMC is a prime target for the study of the early stages of high-mass star formation. We have used Herschel data from the HOBYS key program to produce and analyze column density and temperature maps. Two preliminary catalogs were produced by extracting sources from the column density map and from *Herschel* maps convolved to the 500  $\mu$ m resolution. *Herschel* reveals that among the compact sources (FWHM < 0.45 pc), W3 East, W3 West, and W3 (OH) are the most massive and luminous and have the highest column density. Considering the unique properties of W3 East and W3 West, the only clumps with on-going high-mass star formation, we suggest a ‘convergent constructive feedback’ scenario to account for the formation of a cluster with decreasing age and increasing system/source mass toward the innermost regions. This process, which relies on feedback by high-mass stars to ensure the availability of material during cluster formation, could also lead to the creation of an environment suitable for the formation of Trapezium-like systems. In common with other scenarios proposed in other HOBYS studies, our results indicate that an active/dynamic process aiding in the accumulation, compression, and confinement of material is a critical feature of the high-mass star/cluster formation, distinguishing it from classical low-mass star formation. The environmental conditions and availability of triggers determine the form in which this process occurs, implying that high-mass star/cluster formation could arise from a range of scenarios: from large scale convergence of turbulent flows, to convergent constructive feedback or mergers of filaments.

*Subject headings:* ISM: dust, extinction — ISM: individual (Westerhout 3) — Infrared: stars — Stars: formation — Stars: early-type

## 1. INTRODUCTION

W3 is a  $\sim 4 \times 10^5 M_\odot$  (Moore et al. 2007; Polychroni et al. 2012) Giant Molecular Cloud (GMC) well known for its rich population of H II regions,

clusters, and high-mass star forming sites (see e.g., Megeath et al. 2008 for a detailed description of the field and a review of recent literature). The relatively close distance of W3 ( $\sim 2$  kpc; e.g., Hachisuka et al. 2004; Xu et al. 2006; Navarete et al. 2011) has made this cloud a prime target for the study of cluster/high-mass star formation, which compared to the low-mass case is much less well understood. The question of whether high-mass star formation is simply a scaled-up version of low-mass star formation, or if it is the result of a completely different process (sometimes defined as ‘bimodality’ in star formation), remains one of the main outstanding issues in star formation theory (e.g., Zinnecker & Yorke 2007). Furthermore, while low-mass stars are able to form in isolation, most star formation occurs in clusters embedded in their parent GMCs (Lada & Lada 2003). This situation is particularly true for high-mass stars, making cluster studies crucial to investigating and understanding the origin of high-mass stars.

The W3 GMC was observed with *Herschel* (Pilbratt et al. 2010) as part of the Guaranteed Time Key Program HOBYS<sup>16</sup> (*Herschel* imaging survey of OB Young Stellar objects; Motte et al. 2010). The program is specifically designed to address the major outstanding issues in high-mass star formation with the analysis of all major regions with high-mass stars at distances less than  $d \sim 3$  kpc.

The paper presents a first look at the W3 GMC with

<sup>1</sup> Department of Astronomy and Astrophysics, University of Toronto, 50 St. George Street, Toronto, ON M5S 3H4, Canada

<sup>2</sup> Université de Toulouse, UPS-OMP, IRAP, F-31028 Toulouse cedex 4, France

<sup>3</sup> CNRS, IRAP, 9 Av. colonel Roche, BP 44346, F-31028 Toulouse cedex 4, France

<sup>4</sup> Canadian Institute for Theoretical Astrophysics, University of Toronto, 60 St. George Street, Toronto, ON M5S 3H8, Canada

<sup>5</sup> Department of Astrophysics, Astronomy and Mechanics, Faculty of Physics, University of Athens, Panepistimiopolis, 15784 Zografos, Athens, Greece

<sup>6</sup> Laboratoire AIM, CEA/DSM/Irfu - CNRS/INSU - Université Paris Diderot, CEA-Saclay, F-91191 Gif-sur-Yvette Cedex, France

<sup>7</sup> Univ. Bordeaux, LAB, UMR 5804, F-33270 Floirac, France

<sup>8</sup> CNRS, LAB, UMR 5804, F-33270 Floirac, France

<sup>9</sup> National Research Council Canada, Herzberg Institute of Astrophysics, 5071 West Saanich Road, Victoria, BC, V9E 2E7, Canada

<sup>10</sup> Department of Physics and Astronomy, University of Victoria, PO Box 355, STN CSC, Victoria, BC, V8W 3P6, Canada

<sup>11</sup> INAF-Istituto di Astrofisica e Planetologia Spaziali, via Fosso del Cavaliere 100, I-00133 Rome, Italy

<sup>12</sup> National Astronomical Observatories, Chinese Academy of Sciences, Beijing, China

<sup>13</sup> Department of Physical sciences, The Open University, Milton Keynes, UK

<sup>14</sup> RALspace, The Rutherford Appleton Laboratory, Chilton, Didcot, UK

<sup>15</sup> Department of Physics and Astronomy, McMaster University, Hamilton, ON, L8S 4M1, Canada

<sup>16</sup> <http://www.herschel.fr/cea/hobys/en/>

the recently acquired HOBYS data, focusing on those structures currently hosting the youngest high-mass stars in this field. By identifying and characterizing the properties and origin of these systems, we aim to constrain the pre-requisites for the formation of clusters of high-mass stars. This study is the first of a series of *Herschel*-based papers on W3 currently in preparation, and complements our previous analysis of the YSO content of this field (Rivera-Ingraham et al. 2011) and the study of CO by Polychroni et al. (2012).

This paper is organized as follows. An introduction to the W3 GMC is given in Section 1.1. Section 2 introduces the *Herschel* datasets and images. A global overview of the properties of W3 and its fields as seen by *Herschel* based on the column density and temperature maps is described in Section 3. In Section 4, we focus on the unique properties characteristic of the high-mass star formation in W3 Main. Section 5 outlines a new high-mass formation scenario, described as ‘convergent constructive feedback.’ Our conclusions are summarized in Section 6.

### 1.1. The W3 GMC

W3 contains high-mass stars in various evolutionary stages (e.g., see Tieftrunk et al. 1997). The most active star forming sites are W3 Main, W3 (OH), and AFGL 333. All of these regions (see annotations on Figure 2 below) are located in a prominent and dense structure defined in the literature as the ‘high-density layer’ (HDL; e.g., Oey et al. 2005). The HDL forms the western edge of the W4 ‘Heart Nebula’ bubble, powered by eleven O stars in the cluster IC 1805 ( $2^{\text{h}} 32^{\text{m}} 42^{\text{s}} +61^{\circ} 27'$  (J2000)).

W3 Main contains the most prominent high-mass population of the entire GMC. The two brightest and most central infrared sources in this region, IRS5 and IRS4 (Wynn-Williams et al. 1972), are the youngest high-mass systems in the GMC, as indicated by the presence of numerous hypercompact H II (HCH II) regions (Tieftrunk et al. 1997). IRS5 has been suggested to contain a proto-Trapezium system (Megeath et al. 2005; Rodón et al. 2008) powered by a cluster of OB stars (e.g., Claussen et al. 1994; van der Tak et al. 2005).

The W3 (OH) region is also comprised of two main regions: W3 (OH) itself, a young ultracompact H II (UCH II) region rich in OH masers (Dreher & Welch 1981), and a hot core with a younger massive protobinary system,  $\sim 6''$  east of W3 (OH) (Chen et al. 2006). The region associated with the binary has prominent  $\text{H}_2\text{O}$  emission and it is commonly referred in the literature as W3 ( $\text{H}_2\text{O}$ ) (Little et al. 1977; Turner & Welch 1984).

W3 (OH) and W3 Main are both located in the shell surrounding the cluster IC 1795. This 3 – 5 Myr old cluster is powered by various OB stars, the most massive of which, BD +61°411, has a spectral type O6.5V (Oey et al. 2005). The location of W3 Main and W3 (OH) at the edges of the shell around this cluster has been suggested as evidence for their formation having been induced by IC 1795, itself created by an earlier burst of star formation in the W4 region (Oey et al. 2005). While a triggered origin by IC 1795 appears to be the case for W3 (OH), the characteristics of the cluster of low mass stars associated with W3 Main suggest that this region might actually have begun to form at an ear-

lier stage, prior to IC 1795 (Feigelson & Townsley 2008; Rivera-Ingraham et al. 2011).

KR 140 is a small H II region, 5.7 pc in diameter (Kerton et al. 2001). Located west of the main star-forming activity in the W3 complex and  $\sim 40$  pc SW of IRS5, this H II region is powered by a central and isolated O8.5 star (VES 735) about 1 – 2 Myr old (Ballantyne et al. 2000). Contrary to W3 Main, KR 140 has been suggested to be the result of a rare case of spontaneous high-mass star formation (Ballantyne et al. 2000).

North of KR 140 there is a filamentary-like structure called ‘KR 140-N’ (Rivera-Ingraham et al. 2011) or the ‘Trilobite’ (Polychroni et al. 2010; Polychroni et al. 2012). Its morphology and associated population of young stellar objects (YSOs) suggest the Trilobite could be a case of ‘Radiative Driven Implosion’ (RDI; Rivera-Ingraham et al. 2011), in which an ionization/shock front, such as that driven by an expanding H II region, causes a neighboring overdensity to collapse, triggering the formation of stars.

Several of these prominent features are labeled below in Figures 2 and 3.

### 1.2. Constraining the High-Mass Star Formation Process

Emerging evidence presented in recent studies of several of the HOBYS fields suggests the importance of dynamical processes in high-mass/cluster formation, associated preferentially with filamentary-like regions of high column density of the order of  $N_{\text{H}_2} \sim 10^{23} \text{ cm}^{-2}$  (‘ridges’; Hill et al. 2011; Nguyen Luong et al. 2011a; Hennemann et al. 2012). These structures could be formed by convergence of flows, as proposed for W43 (Nguyen Luong et al. 2011b) and the DR 21 Ridge in Cygnus-X, the latter being one of the most prominent examples (Schneider et al. 2010; Hennemann et al. 2012). The effects of this process in turbulent environments have been investigated extensively in previous studies (e.g., Klessen et al. 2004; Klessen et al. 2005; Heitsch et al. 2006). Other studies of high-mass star forming regions suggest that enhanced accretion at the mergers of filaments is necessary in order to form clusters on short timescales (Dale & Bonnell 2011; Schneider et al. 2012). Such a rapid formation process is required to agree with estimates of the lifetime of the prestellar phase of massive YSOs, which may be as short as a single free-fall time (e.g., Motte et al. 2007).

Questions remain as to whether such models can successfully explain the origin of other known high-mass systems in other regions. If more than one scenario is needed to explain these systems, it is essential to identify the conditions common to all that might constitute the basic requisites for the formation of OB stars and their associated clusters. We return to this in Sections 5 and 6.

## 2. DATA PROCESSING AND *Herschel* IMAGES

W3 was observed by *Herschel* in March 2011. Continuum data were obtained in parallel mode at  $70 \mu\text{m}$  and  $160 \mu\text{m}$  with PACS (Poglitsch et al. 2010), and  $250 \mu\text{m}$ ,  $350 \mu\text{m}$ , and  $500 \mu\text{m}$  with SPIRE (Griffin et al. 2010). The most prominent thermal emission features in W3 are shown in unprecedented detail by the *Herschel* data.

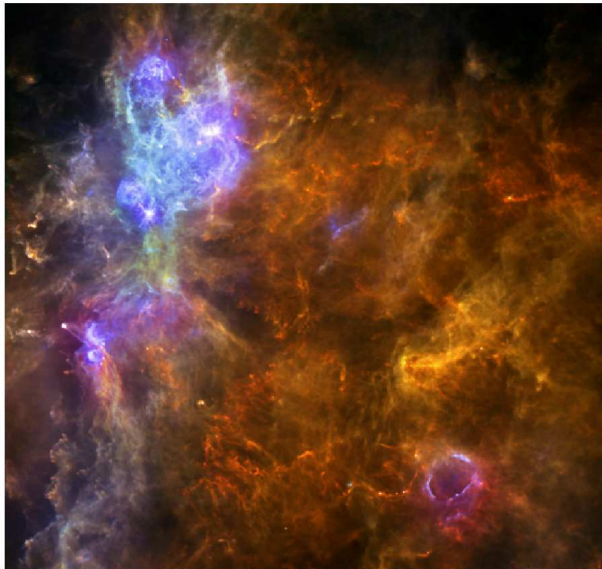


**Figure 1.** Three color image of the W3 GMC using *Herschel* HOBYS data at 70  $\mu\text{m}$  (blue), 160  $\mu\text{m}$  (green) and 250  $\mu\text{m}$  (red). The color tables have been manipulated to bring out the structural detail in the map.

Datasets were reduced from level 0 to level 1 using HIPE v8.1, and the final maps were produced with v17.0 of the Scanamorphos<sup>17</sup> software package (Roussel 2012). Astrometry was corrected using the Two Micron All Sky Survey<sup>18</sup> and *Spitzer* data<sup>19</sup>. The pointing accuracy is estimated to be better than 2". Maps were transformed to MJy/sr and offsets were determined using *Planck* and *IRAS* data (Bernard et al. 2010).

A small saturated area was detected in W3 (OH) at 70, 250, and 350  $\mu\text{m}$  ( $\sim 2^{\text{h}} 27^{\text{m}} 4^{\text{s}} +61^{\circ} 52' 24''$ ). This corresponds to the source IRS8 (Wynn-Williams et al. 1972). Other small (a few pixels) regions were also saturated in W3 Main at 70  $\mu\text{m}$  ( $2^{\text{h}} 25^{\text{m}} 40^{\text{s}}.5 +62^{\circ} 05' 50''$ ) and 250  $\mu\text{m}$  ( $2^{\text{h}} 25^{\text{m}} 40^{\text{s}}.5 +62^{\circ} 05' 50''$ ;  $2^{\text{h}} 25^{\text{m}} 30^{\text{s}}.5 +62^{\circ} 06'$ ). These correspond to the sources IRS5 and IRS4, respectively (Wynn-Williams et al. 1972). These regions were reobserved with *Herschel* using the ‘bright source’ mode. These images showed a good correlation with the originals in the unsaturated areas of overlap and were used to replace the intensities in the saturated pixels.

A three-color image of W3 is shown in Figure 1. The five individual continuum images are presented in Appendix A. Our analysis focuses on the ‘common survey area’,  $\sim 1.5^{\circ}$  in extent in RA and Dec, scanned in two roughly orthogonal directions by PACS and SPIRE according to the telescope focal plane orientation on the date of observation.

Supplementary Stokes I continuum images at 1420 MHz from the Canadian Galactic Plane Survey (CGPS;

Taylor et al. 2003) were used to investigate the location and distribution of the ionized regions.

### 3. COLUMN DENSITY AND DUST TEMPERATURE MAPS

#### 3.1. Data Analysis

To derive column density and dust temperature maps, the PACS and SPIRE maps were first convolved to the resolution at 500  $\mu\text{m}$  ( $\sim 36''$ ;  $\sim 0.35$  pc at a distance of 2 kpc) and projected onto a common  $9'' \text{ pix}^{-1}$  grid (that of the 500  $\mu\text{m}$  map).

The intensities at each pixel were fitted with the approximation<sup>20</sup>

$$I_{\nu} = (1 - \exp(-\tau_{\nu})) B_{\nu}(T), \quad (1)$$

where  $B_{\nu}(T)$  is the Planck function for dust temperature  $T$ . The common assumption in such studies is that  $T$  is constant along the line of sight, obviously a great simplification given the variety of structures and radiation fields. Thus only *Herschel* bands  $\geq 160 \mu\text{m}$  were considered in creating the maps. The optical depth is parametrized as  $\tau_{\nu} = \tau_{\nu_0} (\nu/\nu_0)^{\beta}$  with  $\nu_0 = 1200$  GHz (250  $\mu\text{m}$ ). The optical depth is related to the total H column density by  $\tau_{\nu} = \sigma_{\nu} N_{\text{H}}$  through the opacity  $\sigma_{\nu}$ .

We assumed a fixed dust emissivity index of  $\beta = 2$  and adopted the same opacity standard as in other HOBYS and *Herschel*-based studies (e.g., Motte et al. 2010; André et al. 2010),  $0.1 \text{ cm}^2 \text{ gm}^{-1}$  at 1 THz, equivalently  $\sigma_0 = 3.4 \times 10^{-25} \text{ cm}^2 \text{ H}^{-1}$  using 1.4 as the mean atomic weight per H nucleon. This can be used to deduce the total H column density from  $\tau$ . However, again to be consistent with the scale of column densities in these earlier papers, we used 2.33 rather than 2.8 as the mean atomic weight per molecule, so that what is called  $N_{\text{H}_2}$  is really the column density of ‘mean molecules’ (see also Kauffmann et al. 2008). There is no scaling effect on the mass surface density or the masses of clumps. More importantly, we note that intrinsic uncertainties in the adopted opacity might alter the derived column densities systematically by a factor of  $\sim 2$ , and that there might be systematic differences in opacity across the field or with column density (Martin et al. 2012). Compared to this, photometric calibration errors are relatively small, 15% and 20% for SPIRE and PACS 160  $\mu\text{m}$ , respectively (Griffin et al. 2010; Poglitsch et al. 2010).

Our goal is to assess the column densities and temperature within the W3 GMC itself. The *Herschel* intensities  $I_{\nu}$ , however, contain contributions from dust in the foreground and background, each with its own  $\sigma_{\nu}$ ,  $T$ , and  $N_{\text{H}}$ ; the right hand side of Equation [1] is summed over all components. While a challenging exercise, educated subtraction of the non-GMC components is advantageous for providing a more accurate representation of the true local conditions in the GMC. The process of subtraction is described in Appendix B. Subtracting the foreground and background is most important for characterization of regions where the column density in the GMC is relatively low; it has little effect on the regions of highest column density.

The final corrected column density map is shown in Figure 2. The accompanying temperature map is shown

<sup>20</sup> At the column density peaks (Section 4), the optical depth at 160  $\mu\text{m}$  exceeds 0.3. It is of course even higher at 70  $\mu\text{m}$ , but those data are not used in our assessment.

<sup>17</sup> <http://www2.iap.fr/users/roussel/herschel/index.html>

<sup>18</sup> The Two Micron All Sky Survey (2MASS) is a joint project of the University of Massachusetts and the Infrared Processing and Analysis Center/California Institute of Technology, funded by the National Aeronautics and Space Administration and the National Science Foundation.

<sup>19</sup> <http://irsa.ipac.caltech.edu/applications/Gator/>

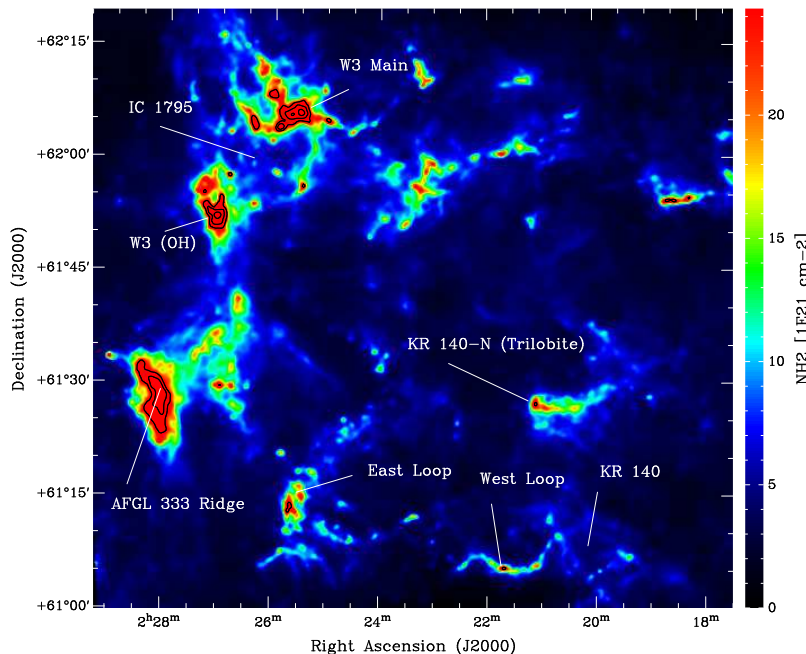


**Figure 2.** Column density map of the W3 GMC after correction for dust emission associated with foreground/background atomic and molecular material, as described in Appendix B. A variety of filaments, pillars and structures are found throughout the GMC. Labels mark prominent features in W3 (Section 1.1). The ‘HDL’ is the dense region comprising W3 Main, W3 (OH), and the AFGL 333 Ridge. Contours are  $N_{\text{H}_2} \approx [30, 60, 200] \times 10^{21} \text{ cm}^{-2}$ .

in Figure 3. Both figures label the most prominent features of the W3 GMC. Unless mentioned otherwise, we used these corrected maps as the default images for our analysis.

For purposes of comparison and discussion, we separate the GMC into four different ‘fields,’ labeled according to their physical location with respect to the center of the entire cloud or a major feature present in the field. The fields are: W3 Main/(OH), W3 NW, AFGL 333, and KR 140 field (see Fig. 3). The W3 Main/(OH) and AFGL 333 fields together comprise what we define as the ‘eastern’ (or HDL) fields in W3, while the other two are the ‘western’ (‘quiescent’ and more ‘diffuse’) ones.

### 3.2. Global Overview

Figure 4 presents the relationship between column density and dust temperature for the four fields, in the form of a two-dimensional histogram. The W3 Main/(OH) field ranges to higher temperatures not observed in the cooler and more diffuse western fields (W3 NW and KR 140). The AFGL 333 field shows a similar high-temperature extension, associated with material at the boundary with W4, but with peak temperatures between those in W3 Main/(OH) and the western fields. In this field there is also low-temperature material, not present in the W3 Main/(OH) field, associated with the structures of the East Loop (Fig. 2), and with properties consistent with those observed in the W3 NW and KR 140 fields.

While most regions in W3 show a clear anticorrelation between high column densities and low temperatures, the Main/(OH) field is unique due to the association of high column densities with warmer temperatures. These structures, warmed by embedded OB stars, are also associated with the youngest high-mass activity in W3 (e.g., W3 Main). This illustrates the difficulty of

**Table 1**  
Global Parameters for the W3 Fields

Field	Mass <sub>unc</sub> <sup>a</sup> [ $10^4 M_{\odot}$ ]	Mass <sup>b</sup> [ $10^4 M_{\odot}$ ]	Area [deg <sup>2</sup> ]	$\Sigma^a$ [ $M_{\odot}/\text{pc}^2$ ]	$\Sigma^b$ [ $M_{\odot}/\text{pc}^2$ ]
Main/(OH)	7.2	6.0	0.43	136	114
AFGL 333	8.1	6.3	0.50	133	103
KR 140	9.4	5.9	0.74	104	65
NW	6.5	4.8	0.53	101	76

<sup>a</sup> Mass and surface density from uncorrected (original) maps.

<sup>b</sup> Mass and surface density corrected for foregr./backgr. material.

using a simple temperature/column density threshold to identify the youngest stages of high-mass star formation in large scale surveys.

Taking into account the material at all temperatures, we find that the four fields, though of unequal area within the common science region, have comparable mass. The main parameters for the four fields, including masses, areas, and surface densities,  $\Sigma$ , for each of the four fields are shown in Table 1. This also includes high column density material above the limits displayed in Figure 4, which belongs mainly to the W3 Main/(OH) field.

The total (all fields) corrected mass of the W3 GMC is found to be  $\sim 2.3 \times 10^5 M_{\odot}$  ( $\sim 3.1 \times 10^5 M_{\odot}$ , uncorrected for foreground-background ISM contribution). This estimate is about half that derived by Polychroni et al. (2012) from molecular data. Moore et al. (2007) found  $\sim 3.8 \times 10^5 M_{\odot}$  from  $^{13}\text{CO}$  for a constant excitation temperature of  $\sim 30 \text{ K}$ . Our mass estimates would be raised (lowered) systematically by adopting a lower (higher) opacity.

### 3.3. Stellar Influence and Cloud Structure

The ionizing and eroding activity of the O stars powering W4 is clearly observed along the eastern edge of our mapped field. The ionization front can be traced in the radio continuum, as shown with Stokes I continuum con-



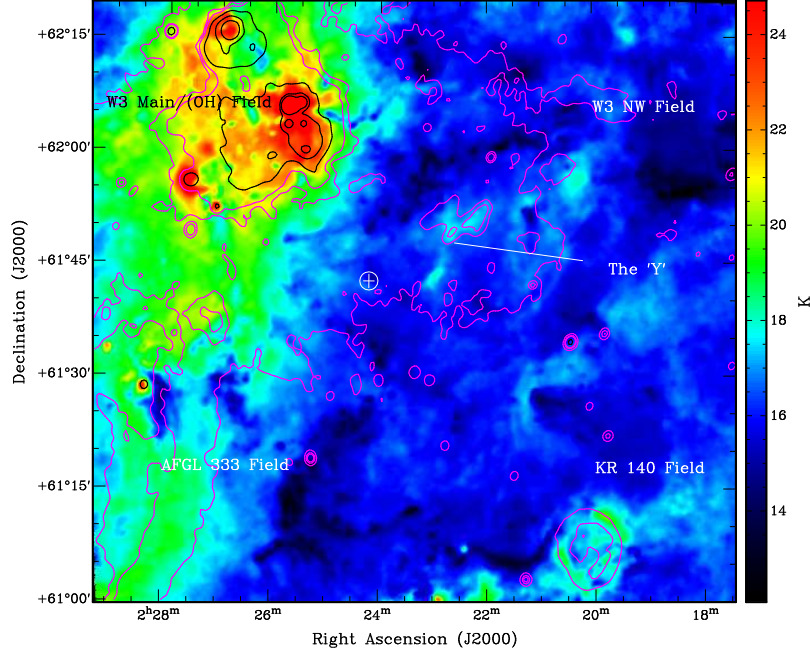


**Figure 3.** Dust temperature map of the W3 GMC after correction for dust emission associated with foreground/background atomic and molecular material, as described in Appendix B. Contours are of Stokes I continuum at 1420 MHz:  $T_b = 8, 12, 15$  K (magenta), and  $T_b = 30, 100$ , and 240 K (black). Colors for contours have been chosen for better contrast in cold and warm regions. White circle with cross marks the intersection of the four fields in W3. From left to right and top to bottom: W3 Main/(OH) field, W3-NW, AFGL 333, KR 140 fields. Figure includes labels for the four fields and the location of the ‘Y’-shaped hot structure (see text).

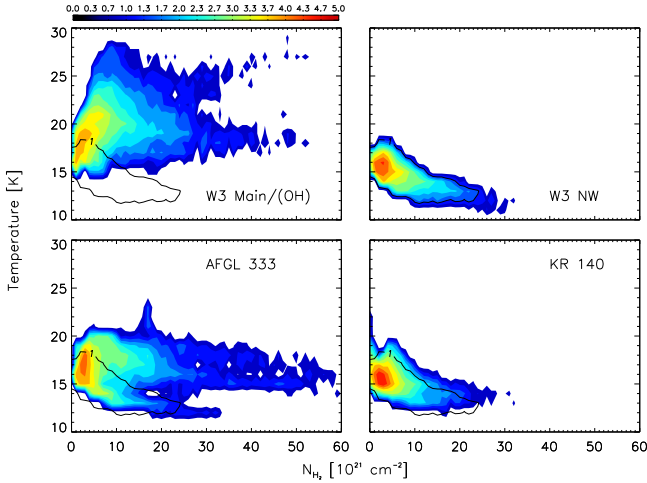


**Figure 4.** Two-dimensional histogram of dust temperature and column density in each W3 field. Color bar indicates number of pixels (log units). Black contour marks the distribution of the W3 NW field as a reference for the distribution in the other fields.

tours in Figure 3. Diffuse radio emission is observed to be most prominent in the HDL, with the strongest peaks coincident with W3 Main, and decreasing progressively into the colder western fields.

Various elongated, dense cloud structures emerging parallel to one another from the HDL are observed to extend more than 10 pc in projection along the boundary with W4, pointing toward the east and the O-star cluster IC 1805 (see Fig. 5). The most prominent of these structures (defined as ‘pillars’ in this work), is located just northeast of AFGL 333 and has signatures of ongoing star formation (Rivera-Ingraham et al. 2011). The location of this structure (P1) and other pillar-regions in W3 are marked below in Figure 5, which shows several

to be part of the coldest structures in the W3 GMC.

There are groups of south-oriented pillars in the central regions of W3, marked P2 and P3 in Figure 5 and seen in more detail in Figure 1 and the original single-band Herschel images in Appendix A. Interaction with W4 alone cannot account for the level of complexity and diversity of such features found west of the HDL; instead they are suggestive of more local stellar influence in the area. Further morphological details and stellar content of the centrally-located (P2, P3) and W4-facing pillars were examined with *Spitzer* images by Rivera-Ingraham et al. (2011).

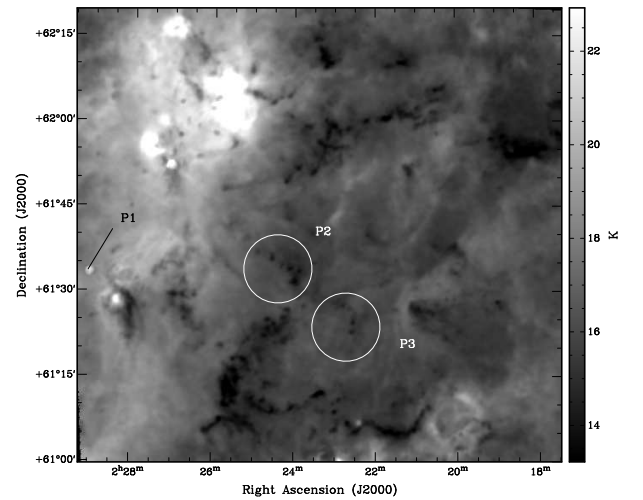


**Figure 5.** Same as Fig. 3, but with intensity and color range modified to highlight the coldest structures. Circles mark the location of pillar-like structures. The IC 1805 cluster is located east of the AFGL 333 Ridge, at  $2^h 32^m 42^s +61^\circ 27'$  (J2000).

Contrary to the HDL and eastern fields, stellar influence in the western fields is very localized, as shown in Figure 3. Examples of these ‘hot’ spots are the KR 140 H II region and a ‘Y’ shape structure (Fig. 3) at  $\sim 2^h 22^m 37^s +61^\circ 49' 41''$ . A bow-shock shaped ‘high’ temperature feature wraps around the eastern side of KR 140-N (Trilobite); displacement in the direction of the YSOs associated with this structure supports a possible case of triggered RDI origin (Rivera-Ingraham et al. 2011).

#### 4. CLUES TO THE ELUSIVE HIGH-MASS STAR FORMATION PROCESS: THE CASE OF W3 MAIN

With the presence of ongoing high-mass star formation and  $N_{\text{H}_2}$  of the order of  $\sim 10^{23} \text{ cm}^{-2}$ , the W3 GMC offers a favorable opportunity to characterize rare high-column density structures and understand how their properties, origin, and evolution might be linked to the onset of high-mass activity.

##### 4.1. Identification of High-Column Density Structures

Figure 6 shows the temperature map of what we define as the ‘AFGL 333 Ridge’ (Fig. 2), in the innermost regions of the AFGL 333 field. It is cold ( $\langle T \rangle \sim 15 \text{ K}$ ,  $T_{\text{min}} \sim 14 \text{ K}$ , for  $N_{\text{H}_2} > 6 \times 10^{22} \text{ cm}^{-2}$ ). The AFGL 333 Ridge is also the only filamentary-shaped structure in the GMC reaching peak column densities of  $\sim 10^{23} \text{ cm}^{-2}$ . This makes it similar to those filaments defined as ‘ridges’ in previous HOBYS papers (e.g., Hill et al. 2011).

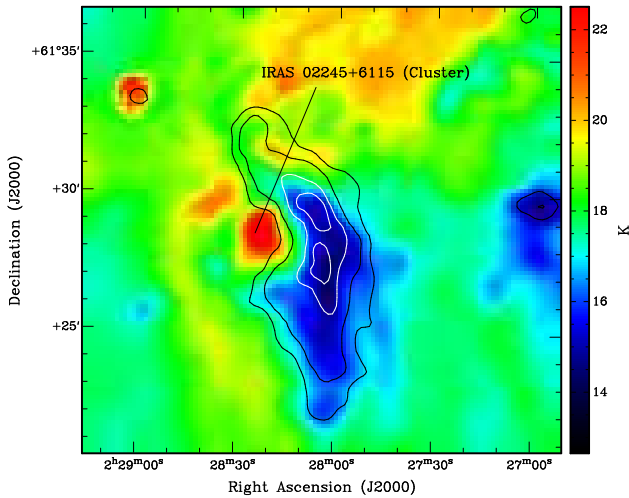


**Figure 6.** Temperature map of the structural details around the central regions of the AFGL 333 field. Black contours are  $N_{\text{H}_2} \approx [20, 30] \times 10^{21} \text{ cm}^{-2}$ . White contours are  $N_{\text{H}_2} \approx [60, 100] \times 10^{21} \text{ cm}^{-2}$ .

Krumholz & McKee (2008) predicted a star formation threshold for high-mass stars of  $\Sigma = 0.7 \text{ g cm}^{-2}$  for a star with  $M \sim 10 M_\odot$ . This surface density corresponds to  $N_{\text{H}_2} \sim 1.8 \times 10^{23} \text{ cm}^{-2}$  in our maps. Although theirs is a specific model, we will for convenience refer to this column density as a ‘massive star formation threshold’ (MSFT). Only three structures in the W3 GMC reach column densities of this order, the W3 East and W3 West clumps (FWHM  $\sim 0.45 \text{ pc}$ ) in W3 Main and W3 (OH) (FWHM  $\sim 0.43 \text{ pc}$ ). Compared to the AFGL 333 Ridge, these are all warm ( $\langle T \rangle \sim 25 \text{ K}$ ,  $T_{\text{min}} \sim 18 \text{ K}$ , for

$N_{\text{H}_2} > 6 \times 10^{22} \text{ cm}^{-2}$ ) as shown in Figures 7 and 8 which concentrate on these most dense regions in the GMC.

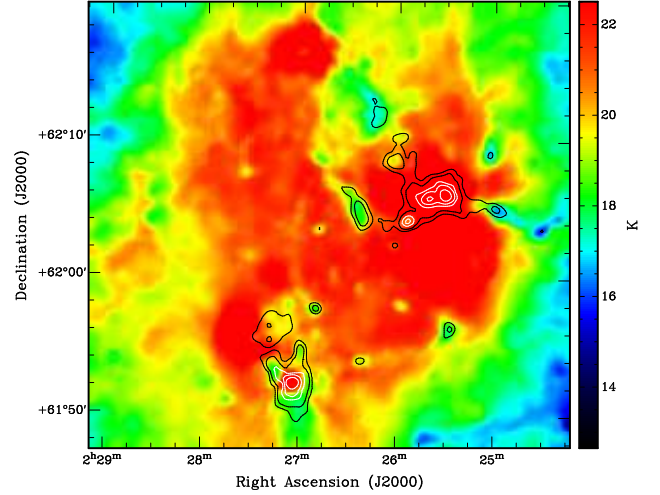


**Figure 7.** Same as Fig. 6, but for W3 Main, W3 (OH), and W3 North with an additional (white) contour at  $N_{\text{H}_2} \approx 200 \times 10^{21} \text{ cm}^{-2}$ .

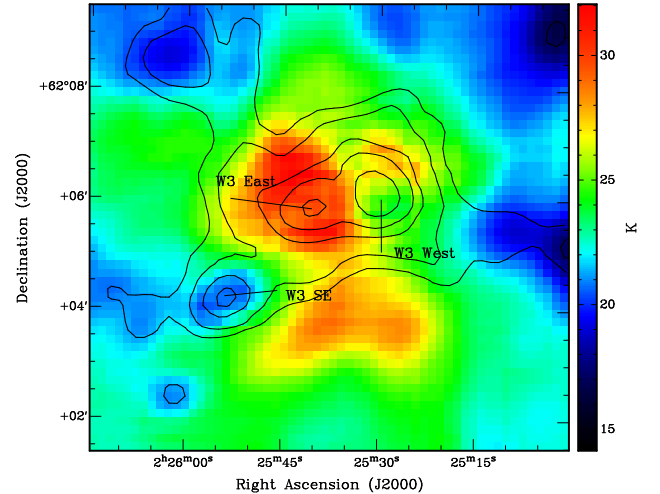


**Figure 8.** Same as Fig. 7, but focusing on the W3 Main region.

The highest column density is in W3 (OH),  $N_{\text{H}_2} \sim [4.5 \pm 1.0] \times 10^{23} \text{ cm}^{-2}$ , comparable within errors to that of W3 West,  $N_{\text{H}_2} \sim [3.3 \pm 0.8] \times 10^{23} \text{ cm}^{-2}$ .

Column densities of this order are consistent with the findings reported by White et al. (1983), Richardson et al. (1989), and the presence of a strong, highly variable water maser in the W3 (OH) region (Little et al. 1977). W3 East is found to have a peak column density 1.4 times lower than W3 West ( $N_{\text{H}_2} \sim [2.3 \pm 0.6] \times 10^{23} \text{ cm}^{-2}$ ), which agrees with the column density ranking of Tiefrunk et al. (1998b) based on molecular  $\text{C}^{18}\text{O}$  data. We note, however, that these authors predict a column density estimate for W3 (OH) from  $\text{NH}_3$  comparable to that of W3 East.

W3 East, W3 West, and W3 (OH) are the only clumps with confirmed ongoing (clustered) high-mass star formation in the W3 GMC, as shown by the presence of masers, HCH II, or UCH II regions. While the MSFT

value is used in this work just as a point of reference when ranking column densities, if such a threshold holds in practice, then a total combined mass of  $\sim 2600 M_{\odot}$  for  $N_{H_2} \geq MSFT$ , about  $\sim 1\%$  of the mass of the W3 GMC, is at present possibly associated with high-mass star formation.

#### 4.2. Masses and Luminosities

As a first reconnaissance, we ran the multi-scale, multi-wavelength source extraction software *getsources* (Men'shchikov et al. 2012; v.1.120828) on the column density map (Fig. 2) made from the *Herschel* images. Some properties of the three most massive clumps associated with the highest column density peaks are summarized in Table 2, assuming a distance of 2.0 kpc. Because *getsources* estimates the local background, the corresponding values above the background, as well as the errors as estimated by *getsources*, are presented. The contributions to the luminosity within the footprint of the structure are evaluated using the mass and  $T$  (Fig. 3) associated with each pixel.

In fitting a modified blackbody, analogous to Equation 1, to the spectral energy distributions (SEDs) from these data, we used  $\beta = 2$  and found the temperature  $T$ , the luminosity  $L$ , and mass  $M$  using the aforementioned opacity. The resulting parameters from our ‘cold’ SED fits ( $\lambda \geq 160 \mu m$ ), and their uncertainties as estimated from Monte Carlo simulations, are included in Table 3.

Ideally one would measure the flux densities by running *getsources* on the original *Herschel* images. However, our choice to use the  $500 \mu m$  resolution for all maps avoids the use of the flux density scaling recipe, used in other HOBYS fields to correct flux densities for the different resolutions prior to fitting the SED, but whose use is only applicable for cores under certain conditions and physical characteristics (Motte et al. 2010; Nguyen Luong et al. 2011a).

All of these estimates are in agreement and confirm that the masses of the  $\sim 0.4 pc$  W3 (OH), W3 West, and W3 East dense clumps are of the order  $\sim 10^3 M_{\odot}$ . These are also in agreement with previous estimates (e.g., Campbell et al. 1995; Tiefrunk et al. 1998b; Megeath et al. 2008 and references therein).

Regardless of the catalog used (that derived from the column density map or the multiband maps) the *Herschel* data indicate that the clumps currently hosting the ongoing high-mass star formation of W3 (W3 East, W3 West, and W3 (OH)) are the most massive and luminous of the entire GMC. Only two sources from the column density source catalog, located in the AFGL 333 Ridge, have a mass of this order (greater than W3 East, albeit less than W3 (OH) and W3 West). They have, however, a lower peak column density and a mean FWHM twice that of the three high extinction sources. Similarly, the only other detection (in addition to W3 (OH) and W3 West) from the convolved multiband catalog with a mass greater than that of W3 East (also associated with the AFGL 333 Ridge), also shows a mean  $FWHM_{500\mu m} \sim 1.5$  times larger. There are no reliably-measured sources with a luminosity reaching that of W3 East, W3 West, or W3 (OH).

#### 4.3. Stellar Content in a Herschel Context

The identification of properties *exclusive* to W3 East, W3 West, and W3 (OH) (structural and stellar content) might reveal clues about their origin and about the general process of high-mass star and cluster formation. Therefore, we attempt here to find some such properties by comparing the *Herschel*-derived results with characteristics of the extensively studied stellar population of the sources in W3 Main (W3 East and W3 West), the only sources in the W3 GMC with recent/ongoing high-mass star formation (containing HCH II regions).

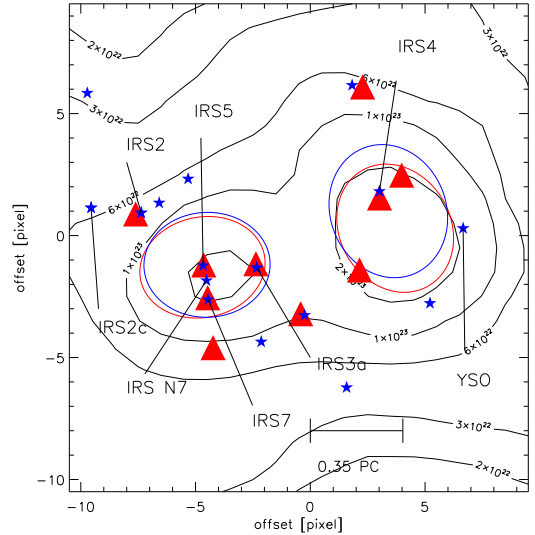


**Table 2**The high extinction structures in the W3 Main/(OH) field: parameters from the  $N_{\text{H}_2}$  and  $T$  maps

Name	RA [h m s]	Dec [ $^{\circ}$ ' '']	Peak $N_{\text{H}_2}^a$ [ $10^{23} \text{ cm}^{-2}$ ]	Peak $T^b$ [K]	Mass [ $10^3 M_{\odot}$ ]	<FWHM> <sup>c</sup> [pc]
W3 West	02 25 30.1	62 06 07	$2.9 \pm 0.8$	$27.2 \pm 2.2$	$1.54 \pm 0.03$	0.45
W3 East	02 25 40.8	62 05 52	$1.8 \pm 0.6$	$30.4 \pm 3.9$	$0.87 \pm 0.03$	0.42
W3 (OH)	02 27 03.7	61 52 21	$4.1 \pm 1.0$	$25.0 \pm 1.9$	$1.85 \pm 0.03$	0.42

<sup>a</sup> Measured at the coordinate center above the local *getsources*-estimated background<sup>b</sup> Measured at the coordinate center.<sup>c</sup> Geometric mean FWHM of elliptical footprint.**Table 3**The high extinction structures in the W3 Main/(OH) field: parameters from SED fitting<sup>a</sup>

Name	RA [h m s]	Dec [ $^{\circ}$ ' '']	Mass [ $10^3 M_{\odot}$ ]	$L$ [ $10^4 L_{\odot}$ ]	$T$ [K]	<FWHM> <sup>b</sup> [pc]	offset <sup>c</sup> [']
W3 West	02 25 30.5	62 06 13	$1.7 \pm 0.5$	$3.5 \pm 1.8$	$24.9 \pm 3.2$	0.46	6.8
W3 East	02 25 40.6	62 05 53	$0.8 \pm 0.3$	$10.3 \pm 9.1$	$32.6 \pm 6.2$	0.42	1.9
W3 (OH)	02 27 03.8	61 52 23	$1.6 \pm 0.5$	$2.3 \pm 1.0$	$23.3 \pm 2.7$	0.42	2.0

<sup>a</sup> Using *getsources* parameters from maps convolved to  $500 \mu\text{m}$  resolution.<sup>b</sup> Geometric mean FWHM of elliptical aperture at  $500 \mu\text{m}$ .<sup>c</sup> Distance from the  $N_{\text{H}_2}$  peak listed in Table 2

by  $\sim 0.5 - 1$ . The YSO and proto-Trapezium system IRS5 is located at the column density peak. Bik et al. (2012) provided no spectral type estimate for IRS5, but our value is compatible with that of IRS3a, the earliest reported star within the FWHM of W3 East, with an estimated spectral type of O5–O7. Also located within the FWHM (boundary), offset  $\sim 0.1$  pc from the column density peak, is IRS7, a late O/early B star associated with an UCH II region and, closer still to the peak ( $\sim 0.05$  pc), IRS N7 (Fig., 9), also a YSO but older than IRS5 (Bik et al. 2012).

Despite the significant population of high-mass stars within its boundaries, W3 East shows evidence of external heating. The highest dust temperatures of the entire GMC ( $\sim 32$  K) are located *outside* the NE and SW boundary of the  $N_{\text{H}_2}$  clump (Fig. 8), and are coincident with the many late O/early B stars  $\lesssim 0.5$  pc from the peak (Fig. 9). These outer stars range in spectral type from early B to O6.5 (IRS2) (Bik et al. 2012).

#### 4.3.2. W3 West

Despite having more mass and higher column density than W3 East, W3 West has a lower dust temperature and is relatively more quiescent. High-mass star formation appears not to have yet progressed or been initiated in the innermost regions; there is no indication of internal high-mass star phenomena coincident with the *Herschel*  $N_{\text{H}_2}$  peak. Corroborating this, there is an  $\text{NH}_3$  peak at the position of the column density peak (Tieftrunk et al. 1998b), and this peak is offset from any PACS (hot) infrared source or any H II region. By contrast, the column density peak of W3 East lacks significant  $\text{NH}_3$  emission suggesting a more advanced state of evolution in which star formation has already influenced the parental cloud locally (Tieftrunk et al. 1998b).

Only IRS4 is found within the boundaries of the W3 West clump,  $\sim 0.1$  pc from the  $N_{\text{H}_2}$  peak (Fig. 9). It is a B0.5–O8 star predicted to be as young as IRS5 based on the presence of HCH II regions (Bik et al. 2012). This is in excellent agreement with the single-star main-sequence (ZAMS) spectral type B0.5 (O9.5) derived from the *Herschel* luminosity of  $L \sim [3.5 \pm 1.8] \times 10^4 L_{\odot}$ .

The other members of the young population of W3 West lie close to or beyond the boundary of the column density structure (Fig. 9). The location of a YSO and other high-mass stars toward the southern and SW boundaries could suggest interaction with the diffuse H II regions at the south.

#### 4.4. High Column Density Structures Lacking High-Mass Star Formation Indicators

In addition to W3 (OH), *Herschel* identifies only two other structures in the W3 GMC with column densities of the order  $N_{\text{H}_2} \sim 10^{23} \text{ cm}^{-2}$ : W3 SE (Fig. 8), in the W3 Main region, and the AFGL 333 Ridge (Fig. 6).

W3 SE is the coolest of the three clumps in W3 Main. It is located  $\sim 1.3$  pc from IRS5, with the closest high-mass star indicator being a diffuse H II region  $< 1$  pc to the southwest.

Also located in the HDL, the AFGL 333 Ridge, despite being at the boundary with W4, shows evidence of a more locally triggered origin. For example, it has:

i) an elongated morphology on the east curved around an embedded cluster *IRAS* 02245+6115 (this cluster is  $\sim 1$  pc from the strongest column density peak in the Ridge and contains a compact H II region powered by a B0.5-type star; e.g., Hughes & Viner 1982);

ii) a distribution of YSOs that follow the curvature of the structure and is abundant in the boundary between the Ridge and the cluster (Rivera-Ingraham et al. 2011); and

iii) an overall much younger population compared to all the other YSO groups in the rest of the field (Rivera-Ingraham et al. 2011). Indeed, the AFGL 333 Ridge contains  $\sim 70\%$  of the Class 0/I population in the AFGL 333 field but only  $\sim 5\%$  of the Class II population (this census excludes the population in the East Loop whose environmental conditions are more consistent with the western fields than the HDL; Rivera-Ingraham et al. 2013, in preparation).

W3 SE and the AFGL 333 Ridge are both forming stars (Rivera-Ingraham et al. 2011) and both appear to have the potential to form high-mass stars. They also have a possible ‘trigger’, i.e., a high-mass star, in their local



neighborhood that could aid in the process. However, they have not reached the column densities, masses, and degree of stellar activity (internal and external to the clumps) characterizing W3 East and W3 West.

#### 5. FORMATION OF CLUSTERS WITH HIGH-MASS STARS AND ‘TRAPEZIUM-LIKE’ SYSTEMS BY ‘CONVERGENT CONSTRUCTIVE FEEDBACK’

A very interesting point noted in previous studies of both W3 East and W3 West (e.g., Tieftrunk et al. 1997; Bik et al. 2012) is a progressive *decrease* in age of the stellar population from the outskirts toward the peak of the density structure, from the farthest diffuse H II regions, to more centrally located evolved compact, and HCH II regions. This is a critical clue. The physical properties inferred from *Herschel* for W3 East and W3 West are unique in the entire W3 GMC. In order to interpret them in the context of their (also unique) geometry, stellar population characteristics, and star formation history, we propose a scenario for formation of a massive clump suitable for hosting a cluster of high-mass stars as well as for formation of the individual high-mass stellar members. We now describe the key features of what we call ‘*convergent constructive feedback*’.

##### 5.1. Key Features

###### 5.1.1. Feedback

Low and high-mass star formation induced (‘triggered’) by external OB stars is a well-studied phenomenon supported by extensive theoretical and observational studies (e.g., White et al. 1999; Tothill et al. 2002; Minier et al. 2009). Local stellar feedback could result in much faster and more efficient star formation than in the quiescent mode at the interaction boundaries between the ‘triggering’ stars and a dense environment (e.g., Elmegreen & Lada 1977).

We might have observed this effect between W4 and the HDL, near AFGL 333 (e.g., Rivera-Ingraham et al. 2011; Rivera-Ingraham et al. 2013, in preparation). Enhanced star formation in triggered regions has also been reported in previous studies (e.g., Thompson et al. 2012; Koenig et al. 2012).

However, the progress of triggering is predicted to be dependent on the environmental conditions. A high-mass star in a dense environment (e.g., a shell or ridge) can only induce further compression only at smaller (sub-parsec) scales; the disruptive effects of newly formed high-mass stars are not efficient in relatively dense regions (Dale & Bonnell 2011) and are therefore of more limited range. Nevertheless, this further compression could propagate the triggering process and the formation of new high-mass stars on the relevant small scales, starting at the boundaries and progressing toward the more dense (inner) regions of the compressed structure. This process would explain, for instance, the presence of molecular cores and condensations at the perimeter of the ionized regions (e.g., Tieftrunk et al. 1995; Tieftrunk et al. 1998a) in W3 Main (W3 East).

While (low/intermediate-mass) star formation likely has taken place in the dense region prior to the present triggering, accounting for the large cluster of low mass stars in the region (Feigelson & Townsley 2008), the rate and efficiency will likely be enhanced at later stages. The

effects of sub-parsec triggering acting within the high column density structure being formed, together with the amount of mass and limited range of the triggering, could sustain lasting periods of star formation in the most central regions, therefore emphasizing the differential age effect.

###### 5.1.2. Constructive

The ‘positive’ effects of stellar feedback by high-mass stars have been studied extensively in the Galaxy, including other HOBYS fields (e.g., Zavagno et al. 2010; Minier et al. 2013, A&A, in press). Here we argue that high-mass stars (‘triggers’) can collectively influence not only the creation of new high-mass stars, but also the new, massive structures hosting this new population of high-mass stars. Indeed, it is a requirement of our scenario that in the dense environment, the progressive formation of high-mass stars will in addition result in the creation of even higher column densities by feedback, rather than simply disruption and dispersal by their mechanical and radiative output.

This is in contrast to alternative models of high-mass cluster formation, like that presented in Peters et al. (2010). In the scenario presented by these authors a central star forms first, followed by the formation of secondary stars in the accretion flow (i.e., star formation propagates outward).

###### 5.1.3. Convergent

To achieve the constructive behavior, we suggest that the *configuration* of the high-mass triggers is a key factor in the formation of the most compact and massive systems (i.e., Trapezium-like systems), like those in W3 Main. When acting on a dense region with enough mass, different populations of high-mass stars with the right ‘confining’ configuration can lead to a ‘convergent’ process, creating/enhancing a central massive structure, moving/trapping the material, and ensuring the availability of mass for accretion during the early otherwise disruptive stages of high-mass star formation. The central column density would continue to grow as new high-mass stars form in a sequential process by sub-parsec triggering at the ‘boundaries’ of the high column density region, where triggering is most effective.

A particularly favorable case could arise where a massive and dense structure is formed *between* separate high-mass star populations, due to their combined effect in compressing and *confining* the material. W3 West exemplifies this possibility. This prominent quiescent column density peak has infrared sources at its periphery, with a clear anticorrelation between molecular and ionized gas (e.g., Tieftrunk et al. 1998b). A similar confining arrangement is also observed for W3 East, and furthermore, higher resolution studies have shown an even smaller central core containing IRS5, within our *Herschel* clump, surrounded by the other H II regions (e.g., Tieftrunk et al. 1995), suggesting that W3 East contains a smaller scale (and already active version) of what is occurring in W3 West. In addition, Tieftrunk et al. (1998b) suggested that the lack of ammonia associated with W3 East was due to NH<sub>3</sub> being ‘thinned out’ or destroyed by ongoing activity *without* dispersal, which also supports the ‘confinement’ aspect of the process. In contrast, an ammonia peak is still present in W3 West. The

combined evidence supports a similar process for both clumps, but with W3 West at an earlier stage.

The concept of convergence is critical for high-mass star/cluster formation as an active process aiding in the continuing supply of material, beyond that required to form a low-mass star. Convergence might arise for a variety of different reasons. Other than our scenario above, evidence for different geometries is presented in recent *Herschel* HOBYS studies for the importance of convergence of flows (Hennemann et al. 2012) and of junctions of filaments (Schneider et al. 2012). In addition to those scenarios aiming to describe the origin of the parsec-scale progenitors of massive clusters, there are various models describing the origin of the individual cluster members. These invoke processes acting at sub-parsec scales, among them small-scale convergence of flows (Csengeri et al. 2011) in addition to turbulent cores (McKee & Tan 2003).

The compression of convergent feedback might also be able to explain the ‘pinched’ morphology of observed magnetic fields (e.g., Roberts et al. 1993; Greaves et al. 1994; Tiefrunk et al. 1995), with an enhancement of the component of the field parallel to the compressed structure (e.g., Peretto et al. 2012).

#### 5.1.4. The combination in W3 Main

A key consequence of the ‘convergent constructive feedback’ process is that stars would form progressively closer to the central regions, each generation ‘aiding’ in the formation of new high-mass stars, and resulting in a systematic *decrease* in age toward the innermost regions of the clump. Returning to our motivation, this behavior is indeed observed in the high-mass stellar population in W3 Main (e.g., Tiefrunk et al. 1997), as well as in the enhanced concentration of young Class 0 stars at the boundaries of the H II regions within the W3 East clump (Ojha et al. 2009) suggestive of induced star formation. Thus the new scenario can account for the unique stellar distribution and characteristics of W3 East and W3 West (spatial, age, and mass distributions, and multiplicity) in conjunction with the *Herschel*-based properties. A sequential process of high-mass star formation in W3 Main was already suggested in previous studies (e.g., Tiefrunk et al. 1997; Feigelson & Townsley 2008: option 4 in their analysis).

#### 5.2. Implications

When trying to address even the most basic processes of the high-mass star formation process, current theoretical models face several challenges such as:

- i) the low core accretion rate  $\dot{m}^*$  (and therefore the long formation times) due to initially low temperatures in the case of the standard protostellar collapse model (e.g.,  $\dot{m}^* \propto T^{3/2}$ ; for isothermal core collapse in the case of spherical collapse; Shu 1977);
- ii) the suppression of accretion due to radiation pressure and ionization by the forming high-mass star (Zinnecker & Yorke 2007);
- iii) formation in clustered environments; and
- iv) primordial mass segregation with anomalous age distributions (e.g., young central massive systems surrounded by a cluster of older low-mass stars).

The ‘convergent constructive feedback’ process might

provide a useful framework for addressing some of these outstanding problems in high-mass star formation.

First, given the age spreads in W3 observed by Bik et al. (2012), a progressive formation of the central column density clump and cluster members must have occurred over a 2 – 3 Myr period. Therefore, there is no need to form such structures fast enough to prevent major internal fragmentation or to invoke long ‘starless’ lifetimes (e.g., several free-fall times; McKee & Tan 2003), which allow for the material to be gathered before the star formation process is initiated (e.g., Zinnecker & Yorke 2007). The ‘older’ halo cluster of low-mass stars surrounding the high-mass star population in W3 Main (e.g., Megeath et al. 1996; Feigelson & Townsley 2008) that formed throughout the region might already have initiated or enhanced the process of compression in the center, as well as contributed to the formation of the first population of high-mass stars.

Second, the simultaneous, small-scale (sub-parsec) triggering by high-mass stars could provide more turbulent, as well as warmer environments. The latter in particular could inhibit fragmentation by increasing the minimum Jeans mass, leading to the formation of new massive cores (e.g., Zinnecker et al. 1993; McKee & Tan 2003; Peters et al. 2010) and an increase in characteristic stellar mass toward the more central regions, as observed for the IRS5 clump for the high and low-mass population (Megeath et al. 1996; Ojha et al. 2009). The combination of high efficiency of triggering and higher temperatures could then be key to the formation and tell-tale characteristics of rich clusters of high-mass stars. The final morphology of the cluster would resemble that of a more evolved cluster after mass segregation. Indeed, from their timescale analysis of W3 Main, Ojha et al. (2009) suggested that the apparent mass segregation must not be dynamical in origin.

Third, when a high-mass star forms close to the central (and most dense) regions of the clump, the limited range of the stellar influence (Dale & Bonnell 2011) and the efficiency of triggering could then lead to the most compact and richest systems, by forming new overdensities, inducing the collapse of preexisting ones, or by direct interaction between the effects of the embedded high-mass stars such as outflows and shocks (Phillips et al. 1988). In W3 East, this could account for the high star formation efficiency and multiplicity observed in the innermost regions of the clump, local to the IRS5 system (Megeath et al. 2005; Rodón et al. 2008). The sub-parsec convergence of flows scenario from Csengeri et al. (2011) would also benefit from the confined environment created by the convergent constructive feedback and/or converging flows, minimizing the disruptive effects.

Fourth, in a scenario with multiple and simultaneous triggering by various high-mass stars, as in W3 Main, the resulting central structure could reach rare, high column densities suitable for the formation of central Trapezium-like systems.

Fifth, the continuing confinement and influence by the high-mass stars at the outer boundaries of clumps could aid the accretion required to produce very massive protostars in the central region, sustaining the feeding process by counteracting or minimizing mass loss due to the stellar outflows, winds, and radiative energy of the newly

formed (and more embedded) high-mass stars. How the actual feeding (accretion) mechanism at in-clump scales proceeds (e.g., in filaments) is, however, beyond the scope (and resolution capabilities) of this work.

In addition to the examples in the W3 GMC, ‘convergent constructive feedback’ might also be responsible for the observed morphology and high-mass star formation in other regions, like the S255-S257 complex (Minier et al. 2007).

### 5.3. W3 (OH) and Other High Column Density Regions

W3 (OH) has an asymmetric cluster spread *along* the tangent to the direction of IC 1795, evidence of direct triggering by IC 1795 itself (e.g., Oey et al. 2005; Feigelson & Townsley 2008). This influence of the IC 1795 is supported by the ‘string’ of stellar clusters extending north of W3 (OH) in the same tangential orientation. There is, however, also evidence of the influence of W4 on the structure containing all of these systems, as observed in the various nebulosities and stars extending from W4 toward the W3 (OH) ‘ridge’/shell (Tieftrunk et al. 1998b), and in the dynamics of this structure and the associated stellar population (e.g., Thronson et al. 1985).

The location of W3 (OH) at the interaction point between the effects of two high-mass populations is therefore more reminiscent of large (parsec) scale convergence of flows, albeit in this case directly powered by high-mass stars rather than large-scale cloud turbulence. Indeed, very large-scale feedback (e.g., over tens of parsecs) might by itself be already capable of enhancing and inducing the collapse of pre-existing structures (e.g., Peretto et al. 2012; Minier et al. 2012 submitted).

Whether ‘convergence of flows’ or ‘convergent constructive feedback’ are responsible, it appears based on the derived *Herschel* properties that similar clumps are produced. However, contrary to W3 Main, W3 (OH) has not benefited from the combined effect of favorable environmental conditions, the efficiency of sub-parsec triggering by (boundary) high-mass stars, and the associated positive effects. This lack of local high-mass stars might explain why, for similar clump mass, the W3 (OH) system is overall less active, and/or why there are two massive clumps with significant high-mass star activity in W3 Main, compared to just one in the ‘shell/ridge’ containing W3 (OH).

On the other hand, W3 SE and the AFGL 333 Ridge have only relatively weak and/or *localized* (one-sided and of scale  $< 1$  pc) high-mass star feedback, driven by isolated late O/early B stars that likely originated from larger-scale stellar feedback from IC 1795 and W4, respectively. Although small-scale (sub-parsec) triggering might have led to the formation of these high column density structures, the collective effects of compression, confinement, and stellar feedback have not (yet) been sufficient to form high-mass stars within them.

## 6. CONCLUSION: A REQUISITE OF HIGH-MASS STAR FORMATION THEORIES

This work is the first analysis of the W3 GMC using the *Herschel* data obtained as part of the Guaranteed Time Key Program HOBYS.

The data were reduced, corrected for contributions from background/foreground material, and used to pro-

duce and analyze the column density and dust temperature maps. The software *getsources* was used to extract a preliminary catalog of compact sources from the column density maps and the *Herschel* maps convolved to the  $500\ \mu\text{m}$  resolution. In particular, the multiband datasets were used to carry out a detailed study of the intrinsic (SED) properties of the clumps currently hosting on-going high-mass star formation, suitable for comparison with the results and suggested high-mass star formation models from other HOBYS fields.

Our results indicate that the  $\sim 0.4$  pc clumps hosting on-going high-mass star formation are unique in the W3 GMC in terms of luminosity, temperature, mass, column density, and stellar content, with W3 East, W3 West, and W3 (OH) being the most massive and the highest column density regions of the entire GMC.

W3 East and W3 West, in addition to W3 (OH), are the only clumps currently forming clusters of high-mass stars in this field. Therefore, we have used the properties *exclusive* to these clumps to develop a scenario linking their ‘extreme’ *Herschel*-based properties with the well-known characteristics of their high-mass stellar content, which are also unique within the W3 GMC.

While numerical models and simulations are required to test the feasibility of different scenarios, we conclude that the observational evidence in W3 points toward a very basic requisite for high-mass star formation: an active and continuing assembly of material for the formation of the most massive cores/clumps. In particular, and in agreement with the conclusions from other HOBYS studies, ‘convergence’ appears to be a common feature for achieving this goal, distinguishing this from low mass star formation. The movement of material would guarantee a build-up of mass and ensure maintenance of the feeding (accretion) process of the massive protostars during their earliest stages despite their disruptive power. A dynamical formation of massive precursors has also been suggested in previous studies based on a statistical analysis of core populations (Motte et al. 2007).

A major difference between the convergence of flows scenario and the scenario proposed here is that we use stellar feedback, the efficiency of triggering in star formation, and the associated displacement, compression, and confinement of material, to ensure the availability of mass during cluster formation. In this process of ‘convergent constructive feedback,’ the sub-parsec influence from different populations of high-mass stars can lead to the creation/enhancement of a massive clump in the most central regions, a suitable precursor of the most massive Trapezium-like systems. In addition there are sequential star formation events initiated at the boundaries of the high-column density structure. This scenario could explain not only the non-dynamical cases of mass segregation, but also those clusters with stellar age decreasing toward the innermost regions of the cluster.

The power, configuration, scale of the triggering process, and the environmental conditions are all likely important in determining the final richness, geometry, timing (e.g., inner young regions versus an outer older population), and the IMF of the formed cluster. Overall, the low probability of satisfying all the prerequisites and conditions for the formation of the most massive clusters could underlie why there are only relatively small numbers of systems like those in Orion, W3 IRS5, and the

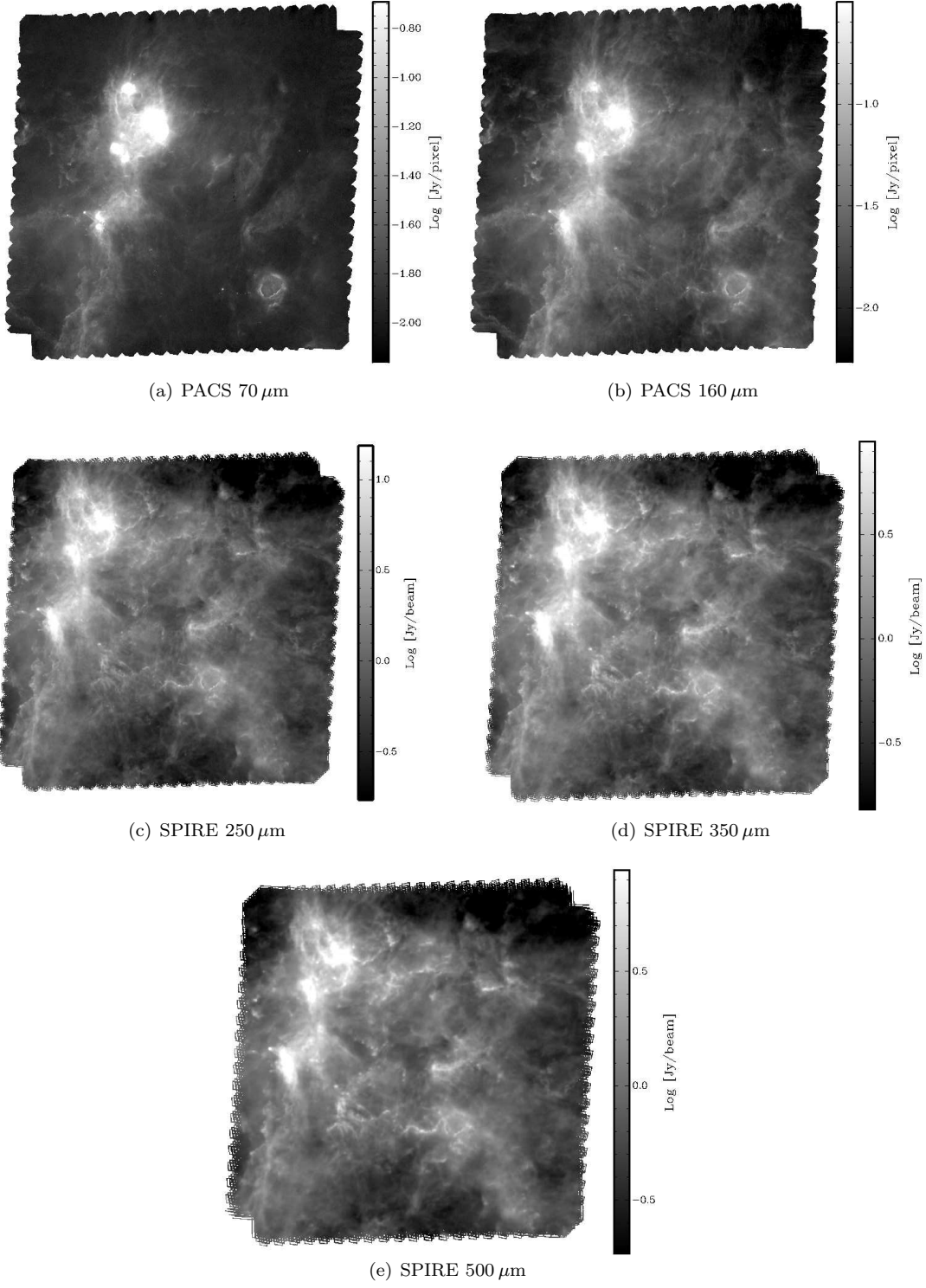
massive clumps in DR 21.

AR-I acknowledges support from an Ontario Graduate Scholarship and a Connaught Fellowship at the University of Toronto. This research was supported in part by the Natural Sciences and Engineering Research Council of Canada and the Canadian Space Agency (CSA). The authors also thank the anonymous referee for his/her useful comments. SPIRE has been developed by a consortium of institutes led by Cardiff Univ. (UK) and including: Univ. Lethbridge (Canada); NAOC (China); CEA, LAM (France); IFSI, Univ. Padua (Italy); IAC (Spain); Stockholm Observatory (Sweden); Imperial College London, RAL, UCL-MSSL, UKATC, Univ. Sussex (UK); and Caltech, JPL, NHSC, Univ. Colorado (USA). This development has been supported by national funding agencies: CSA (Canada); NAOC (China); CEA, CNES, CNRS (France); ASI (Italy); MCINN (Spain); SNSB (Sweden); STFC, UKSA (UK); and NASA (USA). PACS has been developed by a consortium of institutes led by MPE (Germany) and including UVIE (Austria); KU Leuven, CSL, IMEC (Belgium); CEA, LAM (France); MPIA (Germany); INAF-IFSI/OAA/OAP/OAT, LENS, SISSA (Italy); IAC (Spain). This development has been supported by the funding agencies BMVIT (Austria), ESA-PRODEX (Belgium), CEA/CNES (France), DLR (Germany), ASI/INAF (Italy), and CICYT/MCYT (Spain). D.P. is funded through the Operational Program "Education and Lifelong Learning" and is co-financed by the European Union (European Social Fund) and Greek national funds. K.L.J.R. is funded by an ASI fellowship under contract number I/005/11/0.



APPENDIX

A. *HERSCHEL* IMAGES OF W3



## B. CONTRIBUTIONS TO THE *HERSCHEL* INTENSITIES BY DUST ASSOCIATED WITH FOREGROUND/BACKGROUND GAS

While emission in the *Herschel* intensity maps is dominated by the W3 GMC, these maps are still affected by contributions from background and (mainly) foreground material not local to the W3 GMC. To correct for this emission, as done in, e.g., Planck Collaboration et al. (2011b), we need to estimate the contribution  $I_{\nu,i}$  at each *Herschel* band for two contributing components: dust in foreground/background gas that is traced by H I emission (atomic; subscript a) and CO emission (molecular, subscript m). The optically-thin approximation to Equation 1 is sufficient except for the rare high column density peaks where the foreground/background emission is inconsequential, and so  $I_{\nu,i} = \sigma_{\nu,i} B_{\nu}(T_i) N_{H,i}$ .

We used the H I and CO molecular spectral data cubes from the CGPS to estimate the foreground and background contribution. From visual inspection of the CO cube, the velocity range of the W3 GMC is about  $-29$  to  $-60$  km s $^{-1}$ . The foreground/background gas column was therefore estimated by integrating the respective line emission over velocity, *excluding* this range, giving us  $W(\text{H I})_a$  and  $W(\text{CO})_m$ .

For the atomic component, we determined  $N_{H,a}$  by the standard conversion of  $W(\text{H I})_a$  (e.g., Lequeux 2005), ignoring self absorption which would be an uncertain and generally small correction. The few regions that are highly absorbed against the continuum of very bright H II regions were replaced in the column density map by an estimate of the emission using a centered annulus  $3'$  wide; in any case these tend to be high total column density regions where the foreground/background correction is not important.

For the molecular component, we made a preliminary estimate  $N_{H,m} = 2X_{\text{CO}}W(\text{CO})_m$  adopting  $X_{\text{CO}}$  from Strong et al. (1988). In the final analysis, it is actually the product  $\sigma_{\nu,m}X_{\text{CO}}$  that is needed, and we calibrate this below.

The CGPS resolution is only  $\sim 1'$  compared to the  $36''$  required, and these maps have to be interpolated onto the common  $9.0''$  grid of the preliminary *Herschel*-based  $N_{\text{H}_2}$  and  $T$  maps.

### B.1. Parameters for the Foreground/Background Atomic Component

To determine a dust temperature  $T_a$  representative of the atomic gas, we selected regions with  $W(\text{CO}) < 0.5$  K km s $^{-1}$ , low column density in the preliminary column density map (column density below the mean value of the map), the ratio of atomic to molecular ISM contribution greater than one, and with the foreground/background column density greater than the estimated column density in the W3 GMC by at least a factor of five. An example of such a location is the upper left region of the column density map. Pixels in this region of the temperature map are characterized by  $T_a \sim 16$  K, consistent with the lower limit of the temperature range for the atomic material as estimated by Planck Collaboration et al. (2011a,b).

For atomic gas,  $\sigma_{\nu,a}(1200)$  at our fiducial frequency  $\nu_0$  ranges somewhat about a mean  $\sim 1 \times 10^{-25}$  cm $^2$  H $^{-1}$  and  $T \sim 18$  K with  $\beta = 1.8$  (Planck Collaboration et al. 2011a,b). Due to the relatively uniform value of  $N_{H,a}$  over the field, we were unable to calibrate  $\sigma_{\nu,a}(1200)$  ourselves toward this field and so we adopted this value and  $\beta = 1.8$ .

With these parameters, we estimated  $I_{\nu,a}$  across the entire field, and subtracted them from the observed *Herschel* intensities. As a consistency check, we observed that in the regions dominated by the atomic foreground/background, there is no oversubtraction.

### B.2. Parameters for the Foreground/Background Molecular Component

To determine a dust temperature  $T_m$  representative of the molecular gas, we again selected regions of overall low column density and with the foreground/background column density greater than the estimated column density in the W3 GMC by at least a factor of five. Now, however, we required the ratio of atomic to molecular ISM contribution to be less than one and  $W(\text{CO})_m > 3$  K km s $^{-1}$ . An example of such a location is the region below the West Loop. At the positions of these regions we estimated  $T_m \sim 15$  K from the preliminary temperature map.

By correlating  $I_{\nu} - I_{\nu,a}$  (smoothed to  $1'$ ) with  $W(\text{CO})_m$ , we found the slope  $\sigma_{\nu,m}X_{\text{CO}}B_{\nu}(T_m)$  frequency by frequency. This provides a consistency check on the adopted  $T_m$  and  $\beta = 1.8$ . The product  $\sigma_{\nu,m}(1200)X_{\text{CO}}$  was found to be in good agreement for all bands  $\geq 160 \mu\text{m}$  (those used to create the column density maps), with a mean value  $[3.6 \pm 0.3] \times 10^{-5}$  H $^{-1}$  (K km s $^{-1}$ ) $^{-1}$ . We adopted this empirical calibration to estimate  $I_{\nu,m}$  across the entire field. Again we checked for oversubtraction.

If  $X_{\text{CO}} = [2.3 \pm 0.3] \times 10^{20}$  molecules cm $^{-2}$  (K km s $^{-1}$ ) $^{-1}$  from Strong et al. (1988), then  $\sigma_{\nu,m} = [1.6 \pm 0.2] \times 10^{-25}$  cm $^2$  H $^{-1}$ . Planck Collaboration et al. (2011b) estimated  $\sigma_{\nu,m}(1200)$  to be  $2.3 \times 10^{-25}$  cm $^2$  H $^{-1}$  for the molecular phase in the Taurus molecular cloud, within the broad range found in other environments by Martin et al. (2012). If this were the value of the opacity, then  $X_{\text{CO}} = [1.6 \pm 0.2] \times 10^{20}$  molecules cm $^{-2}$  (K km s $^{-1}$ ) $^{-1}$ . Recent results from *Fermi* (Abdo et al. 2010) in the second quadrant find  $X_{\text{CO}} = [1.9 \pm 0.2] \times 10^{20}$  molecules cm $^{-2}$  (K km s $^{-1}$ ) $^{-1}$  in the Perseus arm,  $[1.59 \pm 0.17] \times 10^{20}$  molecules cm $^{-2}$  (K km s $^{-1}$ ) $^{-1}$  in the Local arm, and  $[0.87 \pm 0.05] \times 10^{20}$  molecules cm $^{-2}$  (K km s $^{-1}$ ) $^{-1}$  in more local Gould Belt clouds. For Local arm clouds in the third quadrant,  $X_{\text{CO}} = [2.08 \pm 0.11] \times 10^{20}$  molecules cm $^{-2}$  (K km s $^{-1}$ ) $^{-1}$  (Ackermann et al. 2011).

### B.3. Results

We subtracted the above estimates of  $I_{\nu,a}$  and  $I_{\nu,m}$  from the *Herschel* intensity maps. We then repeated the pixel by pixel SED fitting process using Equation 1 to find the column densities and dust temperatures characteristic of the

W3 GMC itself. For the GMC material, we again adopted the optical depth to column density conversion described in Section 3.1.

On average over the pixels in the map, the foreground/background correction decreases the observed column densities by  $\sim 30 \pm 15\%$ , with a greater proportional effect on the lower column density regions and little effect on the high column density peaks and ridges.

We note that some ‘artifacts’ might inevitably appear in areas in which the foreground/background dominates: after the subtraction the residual intensity is quite small, whereas the errors remain, so that it is difficult to obtain a reliable fit. The main region suffering from this effect is located south of the West Loop, where the relatively prominent foreground/background CO component was used to calibrate the opacity. Here, the intensity correction has produced a prominent feature in Figure 3 near  $2^{\text{h}} 22^{\text{m}} 50^{\text{s}}, +61^{\circ} 0' 40''$ , which also produces the spike in  $T$  at low column densities seen in the panel for KR 140 in Figure 4. Such regions could be masked for any analysis sensitive to details at low column densities, particularly because these are most prone to other systematic errors, including uncertainties in the offsets added to the *Herschel* maps derived from *Planck* and *IRAS*, uncertainties in the map-making techniques, use of the same  $\sigma_{\nu,i}$  and  $T_i$  for all of the dust in the foreground and background gas components, and optical depth effects in the gas tracers across the field.

## REFERENCES

- Abdo, A. A., Ackermann, M., Ajello, M., et al. 2010, *ApJ*, 710, 133  
 Ackermann, M., Ajello, M., Baldini, L., et al. 2011, *ApJ*, 726, 81  
 André, P., Men’shchikov, A., Bontemps, S., et al. 2010, *A&A*, 518, L102  
 Ballantyne, D. R., Kerton, C. R., & Martin, P. G. 2000, *ApJ*, 539, 283  
 Bernard, J.-P., Paradis, D., Marshall, D. J., et al. 2010, *A&A*, 518, L88  
 Bik, A., Henning, T., Stolte, A., et al. 2012, *ApJ*, 744, 87  
 Campbell, M. F., Butner, H. M., Harvey, P. M., et al. 1995, *ApJ*, 454, 831  
 Chen, H.-R., Welch, W. J., Wilner, D. J., & Sutton, E. C. 2006, in *Astronomical Society of the Pacific Conference Series*, Vol. 356, *Revealing the Molecular Universe: One Antenna is Never Enough*, ed. D. C. Backer, J. M. Moran, & J. L. Turner, 270  
 Claussen, M. J., Gaume, R. A., Johnston, K. J., & Wilson, T. L. 1994, *ApJ*, 424, L41  
 Csengeri, T., Bontemps, S., Schneider, N., Motte, F., & Dib, S. 2011, *A&A*, 527, A135  
 Dale, J. E., & Bonnell, I. 2011, *MNRAS*, 414, 321  
 Dreher, J. W., & Welch, W. J. 1981, *ApJ*, 245, 857  
 Elmegreen, B. G., & Lada, C. J. 1977, *ApJ*, 214, 725  
 Feigelson, E. D., & Townsley, L. K. 2008, *ApJ*, 673, 354  
 Greaves, J. S., Murray, A. G., & Holland, W. S. 1994, *A&A*, 284, L19  
 Griffin, M. J., Abergel, A., Abreu, A., et al. 2010, *A&A*, 518, L3+  
 Hachisuka, K., Brunthaler, A., Hagiwara, Y., et al. 2004, in *European VLBI Network on New Developments in VLBI Science and Technology*, ed. R. Bachiller, F. Colomer, J.-F. Desmurs, & P. de Vicente, 317  
 Heitsch, F., Slyz, A. D., Devriendt, J. E. G., Hartmann, L. W., & Burkert, A. 2006, *ApJ*, 648, 1052  
 Hennemann, M., Motte, F., Schneider, N., et al. 2012, *A&A*, 543, L3  
 Hill, T., Motte, F., Didelon, P., et al. 2011, *A&A*, 533, A94  
 Hughes, V. A., & Viner, M. R. 1982, *AJ*, 87, 685  
 Kauffmann, J., Bertoldi, F., Bourke, T. L., Evans, II, N. J., & Lee, C. W. 2008, *A&A*, 487, 993  
 Kerton, C. R., Martin, P. G., Johnstone, D., & Ballantyne, D. R. 2001, *ApJ*, 552, 601  
 Klessen, R. S., Ballesteros-Paredes, J., Li, Y., & Mac Low, M.-M. 2004, in *Astronomical Society of the Pacific Conference Series*, Vol. 322, *The Formation and Evolution of Massive Young Star Clusters*, ed. H. J. G. L. M. Lamers, L. J. Smith, & A. Nota, 299  
 Klessen, R. S., Ballesteros-Paredes, J., Vázquez-Semadeni, E., & Durán-Rojas, C. 2005, *ApJ*, 620, 786  
 Koenig, X. P., Leisawitz, D. T., Benford, D. J., et al. 2012, *ApJ*, 744, 130  
 Krumholz, M. R., & McKee, C. F. 2008, *Nature*, 451, 1082  
 Lada, C. J., & Lada, E. A. 2003, *ARA&A*, 41, 57  
 Lequeux, J. 2005, *The Interstellar Medium*, ed. Lequeux, J.  
 Little, L. T., White, G. J., & Riley, P. W. 1977, *MNRAS*, 180, 639  
 Martin, P. G., Roy, A., Bontemps, S., et al. 2012, *ApJ*, 751, 28  
 Martins, F., Schaerer, D., & Hillier, D. J. 2005, *A&A*, 436, 1049  
 McKee, C. F., & Tan, J. C. 2003, *ApJ*, 585, 850  
 Megeath, S. T., Herter, T., Beichman, C., et al. 1996, *A&A*, 307, 775  
 Megeath, S. T., Townsley, L. K., Oey, M. S., & Tiefertunk, A. R. 2008, *Low and High Mass Star Formation in the W3, W4, and W5 Regions*, ed. Reipurth, B., 264 +  
 Megeath, S. T., Wilson, T. L., & Corbin, M. R. 2005, *ApJ*, 622, L141  
 Men’shchikov, A., André, P., Didelon, P., et al. 2012, *A&A*, 542, A81  
 Minier, V., Peretto, N., Longmore, S. N., et al. 2007, in *IAU Symposium*, Vol. 237, *IAU Symposium*, ed. B. G. Elmegreen & J. Palous, 160–164  
 Minier, V., André, P., Bergman, P., et al. 2009, *A&A*, 501, L1  
 Moore, T. J. T., Bretherton, D. E., Fujiyoshi, T., et al. 2007, *MNRAS*, 379, 663  
 Motte, F., Bontemps, S., Schilke, P., et al. 2007, *A&A*, 476, 1243  
 Motte, F., Zavagno, A., Bontemps, S., et al. 2010, *A&A*, 518, L77  
 Navarete, F., Figueredo, E., Damineli, A., et al. 2011, *AJ*, 142, 67  
 Nguyen Luong, Q., Motte, F., Hennemann, M., et al. 2011a, *A&A*, 535, A76  
 Nguyen Luong, Q., Motte, F., Schuller, F., et al. 2011b, *A&A*, 529, A41  
 Oey, M. S., Watson, A. M., Kern, K., & Walth, G. L. 2005, *AJ*, 129, 393  
 Ojha, D. K., Tamura, M., Nakajima, Y., et al. 2009, *ApJ*, 693, 634  
 Panagia, N. 1973, *AJ*, 78, 929  
 Peretto, N., André, P., Könyves, V., et al. 2012, *A&A*, 541, A63  
 Peters, T., Banerjee, R., Klessen, R. S., et al. 2010, *ApJ*, 711, 1017

- Phillips, J. P., White, G. J., Rainey, R., et al. 1988, *A&A*, 190, 289
- Pilbratt, G. L., Riedinger, J. R., Passvogel, T., et al. 2010, *A&A*, 518, L1
- Planck Collaboration, Abergel, A., Ade, P. A. R., et al. 2011a, *A&A*, 536, A24
- . 2011b, *A&A*, 536, A25
- Poglitsch, A., Waelkens, C., Geis, N., et al. 2010, *A&A*, 518, L2+
- Polychroni, D., Moore, T. J. T., & Allsopp, J. 2010, in *Astronomical Society of the Pacific Conference Series*, Vol. 424, 9th International Conference of the Hellenic Astronomical Society, ed. K. Tsinganos, D. Hatzidimitriou, & T. Matsakos, 165–+
- Polychroni, D., Moore, T. J. T., & Allsopp, J. 2012, *MNRAS*, 422, 2992
- Richardson, K. J., White, G. J., Sandell, G., Duncan, W. D., & Krisciunas, K. 1989, *A&A*, 221, 95
- Rivera-Ingraham, A., Martin, P. G., Polychroni, D., & Moore, T. J. T. 2011, *ApJ*, 743, 39
- Rivera-Ingraham, A., Ade, P. A. R., Bock, J. J., et al. 2010, *ApJ*, 723, 915
- Roberts, D. A., Crutcher, R. M., Troland, T. H., & Goss, W. M. 1993, *ApJ*, 412, 675
- Rodón, J. A., Beuther, H., Megeath, S. T., & van der Tak, F. F. S. 2008, *A&A*, 490, 213
- Roussel, H. 2012, *arXiv:1205.2576*
- Schneider, N., Csengeri, T., Bontemps, S., et al. 2010, *A&A*, 520, A49
- Schneider, N., Csengeri, T., Hennemann, M., et al. 2012, *A&A*, 540, L11
- Shu, F. H. 1977, *ApJ*, 214, 488
- Strong, A. W., Bloemen, J. B. G. M., Dame, T. M., et al. 1988, *A&A*, 207, 1
- Taylor, A. R., Gibson, S. J., Peracaula, M., et al. 2003, *AJ*, 125, 3145
- Thompson, M. A., Urquhart, J. S., Moore, T. J. T., & Morgan, L. K. 2012, *MNRAS*, 421, 408
- Thronson, Jr., H. A., Lada, C. J., & Hewagama, T. 1985, *ApJ*, 297, 662
- Tieftrunk, A. R., Gaume, R. A., Claussen, M. J., Wilson, T. L., & Johnston, K. J. 1997, *A&A*, 318, 931
- Tieftrunk, A. R., Gaume, R. A., & Wilson, T. L. 1998a, *A&A*, 340, 232
- Tieftrunk, A. R., Megeath, S. T., Wilson, T. L., & Rayner, J. T. 1998b, *A&A*, 336, 991
- Tieftrunk, A. R., Wilson, T. L., Steppe, H., et al. 1995, *A&A*, 303, 901
- Tothill, N. F. H., White, G. J., Matthews, H. E., et al. 2002, *ApJ*, 580, 285
- Turner, J. L., & Welch, W. J. 1984, *ApJ*, 287, L81
- van der Tak, F. F. S., Tuthill, P. G., & Danchi, W. C. 2005, *A&A*, 431, 993
- White, G. J., Richardson, K. J., Frost, R. F., et al. 1983, *MNRAS*, 204, 1117
- White, G. J., Nelson, R. P., Holland, W. S., et al. 1999, *A&A*, 342, 233
- Wynn-Williams, C. G., Becklin, E. E., & Neugebauer, G. 1972, *MNRAS*, 160, 1
- Xu, Y., Reid, M. J., Zheng, X. W., & Menten, K. M. 2006, *Science*, 311, 54
- Zavagno, A., Anderson, L. D., Russeil, D., et al. 2010, *A&A*, 518, L101
- Zinnecker, H., McCaughrean, M. J., Rayner, J. T., Wilking, B. A., & Moneti, A. 1993, in *Reviews in Modern Astronomy*, Vol. 6, *Reviews in Modern Astronomy*, ed. G. Klare, 191–208
- Zinnecker, H., & Yorke, H. W. 2007, *ARA&A*, 45, 481